Highly stable heterostructured Ag–AgBr/TiO 2 composite: A bifunctional visible-light active photocatalyst for destruction of ibuprofen and bacteria

ARTICLE *in* JOURNAL OF MATERIALS CHEMISTRY · OCTOBER 2012

Impact Factor: 7.44 · DOI: 10.1039/C2JM35503E

4 AUTHORS, INCLUDING:

Yuxin Tang
Nanyang Technological University
63 PUBLICATIONS **1,209** CITATIONS
SEE PROFILE

Teik Thye (T-T) Lim
Nanyang Technological University
108 PUBLICATIONS **3,240** CITATIONS
SEE PROFILE

Journal of Materials Chemistry

Cite this: DOI: 10.1039/c2jm35503e

www.rsc.org/materials

PAPER

Highly stable heterostructured Ag–AgBr/TiO_2 composite: a bifunctional visible-light active photocatalyst for destruction of ibuprofen and bacteria†

Xiaoping Wang,[a] Yuxin Tang,[b] Zhong Chen[b] and Teik-Thye Lim*[a]

Received 14th August 2012, Accepted 12th September 2012
DOI: 10.1039/c2jm35503e

A bifunctional visible-light photocatalyst Ag–AgBr/TiO_2 was synthesized by a facile one-pot method. The three-component composite exhibited much superior visible-light photocatalytic activities for ibuprofen (IBP) degradation and mineralization as compared to single-component (TiO_2) and two-component (Ag/TiO_2, Ag–AgBr) systems, as well as the conventional Ag–AgBr/P25. After 6 h of white LED irradiation, 81% of organic carbon could be mineralized along with decreased aromaticity and toxicity of the IBP degradation products. Meanwhile, the synthesized Ag–AgBr/TiO_2 exhibited much stronger antibacterial activities than TiO_2 and conventional Ag–AgBr/P25 under white LED irradiation. More interestingly, the Ag–AgBr/TiO_2 had novel antibacterial activities against *E. coli* in the dark as compared to other Ag–AgBr/semiconductor photocatalysts that have been reported. For the first time, the action spectrum of Ag–AgBr/TiO_2 was investigated using different colors of LED to elucidate the roles of Ag nanoparticles and AgBr in its visible-light photocatalytic activity. It reveals that both AgBr and Ag nanoparticles were photoactive species contributing to the high photocatalytic performance. Among the various oxidative species (h^+, $^{\cdot}OH$, $O_2^{\cdot-}$ and $^1O_2$), $O_2^{\cdot-}$ was the predominant species involved in IBP degradation upon the Ag–AgBr/TiO_2 under white LED irradiation. The visible-light photocatalytic mechanism of Ag–AgBr/TiO_2 and factor contributing to its high photostability in water are proposed.

1. Introduction

TiO_2 appears to be the most promising and suitable photocatalyst for use in water and wastewater treatment. However, the widespread application of TiO_2 has been greatly restricted due to its inefficient utilization of solar energy. Various strategies have been explored to modify the TiO_2 so that it can be photoresponsive under visible light, such as doping with metals and non-metals, surface sensitization with organic dyes, and coupling with narrow band gap semiconductors.[1–3] Recently, plasmonic photocatalysts consisting of Ag nanoparticles have attracted increasing attention in the field of visible-light photocatalysis.[4–7] It has been accepted that visible light incident upon the surface of Ag nanoparticles can induce collective oscillations of the conduction electrons with a resonant frequency, commonly known as localized surface plasmon resonance (SPR).[8] As a result of the SPR property, Ag nanoparticles exhibit strong absorption of visible light.[9] In particular, Ag–AgX (X = Cl, Br) structures have been found to be the stable and highly efficient photocatalysts under visible light irradiation.[4,10]

More recently, the Ag–AgX structures have been frequently used for constructing the heterostructured multi-semiconductor systems to extend the light-response range to the visible light region.[11–14] Moreover, the heterostructuring could promote the separation of photoexcited electron–hole pairs within these components.[2,11,15] Hu *et al.* used Degussa P25 as the support for Ag–AgBr through the deposition–precipitation method. In this system, AgBr was the main active species for destruction of azodyes and bacteria under visible light irradiation, whereas the existence of surface metallic Ag possibly enhanced the electron–hole separation and improved the stability of AgBr.[16] Tian *et al.* synthesized tubular composites of TiO_2 tube-supported Ag–AgBr nanoparticles. The formation of nanojunctions in these composites resulted in the effective migration of photoinduced carriers at the interface, leading to the enhanced photocatalytic activity in degradation of phenol under simulated solar-light irradiation as compared to the particulate Ag–AgBr/P25.[17] The plasmonic photocatalysts have also been synthesized by immobilization of Ag–AgX nanoparticles on a TiO_2 thin film with uniform dispersion, which exhibited good visible-light

[a]*Division of Environmental and Water Resources Engineering, School of Civil and Environmental Engineering, Nanyang Technological University, Singapore 639798, Singapore. E-mail: cttlim@ntu.edu.sg; Fax: +65 67910676; Tel: +65-6790-6933*
[b]*School of Materials Science and Engineering, Nanyang Technological University, Singapore 639798, Singapore*

† Electronic supplementary information (ESI) available: FESEM images of reference samples, TEM images of Ag–AgBr/TiO_2 composites combined with EDX spectra, time-dependent UV-vis absorption spectra and HPLC profiles of IBP, comparison of XRD and XPS results of fresh and used Ag–AgBr/TiO_2, photocatalytic mechanisms over Ag/TiO_2 and Ag–AgBr under white LED irradiation. See DOI: 10.1039/c2jm35503e

photocatalytic activity and stability for degradation of methyl orange.[11,18] Generally, the previous studies show that the multi-step synthetic procedures involving fabrication of TiO_2 nanotubes and subsequent deposition of Ag–AgBr on the TiO_2 nanotubes are relatively complex and time-consuming. On the other hand, direct deposition of Ag–AgX onto P25 would cause serious aggregations, and it is difficult to achieve the effective interaction between the components.

Herein, we describe a facile one-pot method to synthesize Ag–AgBr/TiO_2 composites of high photostability that consist of Ag–AgBr nanoparticles homogenously dispersed in the matrix of TiO_2 particles. The effect of the synthetic procedure on the resulting Ag–AgBr/TiO_2 composites was studied. The visible-light photocatalytic activity for degradation of a biorecalcitrant organic pollutant ibuprofen (IBP) was investigated. IBP is a non-steroidal anti-inflammatory drug (NSAID) often used against fever, musculature pain and inflammatory disorders, and conventional wastewater treatment processes often fail to effectively remove it.[19,20] Furthermore, total organic carbon (TOC), degree of aromaticity of byproducts and toxicity of the IBP solutions were investigated during the course of photocatalytic process. Antibacterial activities of Ag–AgBr/TiO_2 against *E. coli* in the dark and under white LED irradiation were also studied. Finally, the possible mechanisms for the high stability and visible-light photocatalytic activity of the Ag–AgBr/TiO_2 are proposed.

2. Experimental

2.1 Synthesis of Ag–AgBr/TiO_2 composites

2.1.1 Preparation of AgBr/TiO_2 *via* sol–gel route. Firstly, solution A (45 mL) containing 0.16 g of $AgNO_3$ (≥98%, Merck) and 2 mL of ammonia (25 wt%, Merck) and solution B (45 mL) consisting of 0.91 g of cetyltrimethylammonium bromide (CTAB, ≥98%, Merck) were prepared with ethanol (99.5–99.8%, Merck). 2.98 mL of titanium isopropoxide (TTIP, ≥98%, Merck) was further added to solution B. The mixture of these two solutions was stirred continuously for 3 h at room temperature. The resulting light yellow gel was then dried at 70 °C overnight and calcined at 450 °C for 2 h.

2.1.2 Preparation of AgBr/TiO_2 *via* solvothermal route. The mixture of solutions containing $AgNO_3$, CTAB and TTIP were prepared following the above procedure. It was then transferred into a 125 mL Teflon-lined stainless steel autoclave, followed by solvothermal treatment at 150 °C for 4 h. The product was separated by centrifugation, thoroughly washed with deionized (DI) water, dried at 70 °C overnight and further calcined at 450 °C for 2 h.

2.1.3 Preparation of Ag–AgBr/TiO_2. The obtained yellow powders of AgBr/TiO_2 were dispersed into DI water under vigorous stirring and white LED irradiation for 2 h. The product was then collected and dried at 70 °C. The gray Ag–AgBr/TiO_2 and S–Ag–AgBr/TiO_2 (S refers to solvothermal) photocatalysts were finally obtained respectively.

2.1.4 Preparation of reference samples. For comparison, other types of samples were also prepared. Pure TiO_2 was prepared by the above sol–gel method. Ag/TiO_2 was prepared by following the procedure of Ag–AgBr/TiO_2 synthesis but without introducing CTAB. Ag–AgBr was synthesized *via* solvothermal treatment at 120 °C for 8 h followed by photoreduction route without TTIP. Meanwhile, Ag–AgBr/P25 was prepared by the deposition–precipitation method as follows. 1 g of P25 was added to 80 mL of DI water. 1.2 g of CTAB was further added to the suspension after it was under sonication for 30 min. The mixture was stirred for another 30 min until CTAB was completely dissolved. Solution of $AgNO_3$ (0.21 g) and ammonia (25 wt%, 2 mL) in DI water was then added into the mixture and stirred for 3 h. The subsequent procedure was similar to preparation of Ag–AgBr/TiO_2.

2.2 Materials characterization

X-ray diffraction (XRD) patterns were collected using a Bruker D8 Advance X-ray diffractometer with monochromated high-intensity Cu Kα radiation ($\lambda = 1.5418$ Å) in a 2θ range of 5–80°. X-ray photoelectron spectroscopy (XPS) studies were conducted on a Krato Axis Ultra spectrometer with a monochromatic Al Kα excitation source ($h\nu = 1486.71$ eV). The binding energies (BE) were calibrated using C 1s core level at 284.8 eV for the adventitious carbon as reference. Field emission scanning electronic microscope (FESEM, JEOL JSM-6340F) and transmission electron microscopy (TEM, JEOL JEM-2010) were used to study the nanostructures. Energy dispersive X-ray analysis (EDX) attached to FESEM or TEM was also carried out. The UV-vis diffuse reflectance spectra (DRS) were recorded on a UV-vis spectrometer (Lambda 35, Perkin-Elmer). The Brunauer–Emmett–Teller surface area (S_{BET}) was measured by a Quantachrome Autosorb-1 system using N_2 adsorption/desorption at liquid-nitrogen temperature (77 K). Photoluminescence (PL) emission spectra of the samples were recorded at room temperature using a SPEX Fluorolog-3 spectrometer (Horiba Scientific, New Jersey, USA) with excitation wavelength at 320 nm.

2.3 Evaluation of photocatalytic activity and antibacterial activity

Stock solution of IBP (≥98%, Sigma) was prepared with DI water. The preparation was carried out at the ambient (unadjusted) pH. Photocatalytic experiments were performed in a Vis-LED photoreactor as described in our previous work.[21] In a typical experiment, a 200 mL suspension containing photocatalysts (dosage = 0.5 g L^{-1}) and IBP (10 mg L^{-1}) was stirred in the dark for 1 h to establish adsorption/desorption equilibrium of IBP on the photocatalyst surface. Aliquots of solution were collected at designated time intervals and filtered using membrane filters (0.45 μm pore size).

The IBP concentration was determined by a high-performance liquid chromatograph (HPLC, Perkin-Elmer Series200), which comprised a Series 200 UV/Vis detector and C18 column (5 μm, 150 × 4.6 mm, Inertsil ODS-3 column). The TOC remained in the solutions was measured using a Shimadzu ASI-V TOC analyzer. The final ionic products of IBP degradation were monitored by ion chromatograph (IC, Dionex ICS-1000). The toxicity of IBP solution during the photocatalytic process was evaluated using a Microtox toxicity test system (Azur Microtox

Analyzer Model 500) which is based upon the use of a bioluminescent marine bacterium (*Vibrio fischeri*). The inhibition of bioluminescence of *V. fischeri* after 15 min exposure to the samples was measured. Microtox test for each sample was performed in triplicate at least. The inhibition percentage was obtained to reflect the toxicity level of the test sample.[22] The degree of aromaticity of the byproducts, whose reduction indicates the extent of ring-opening reaction for IBP, was determined based on UV absorption at 254 nm (UV254) using a UV-vis spectrometer (Lambda 35, Perkin-Elmer).

Antibacterial activities of the prepared photocatalysts against *E. coli* in the dark and under visible-light LED irradiation were also investigated. 100 mL suspension containing *E. coli* ($\sim 2 \times 10^7$ CFU mL^{-1}) and photocatalysts was used. An aliquot of the reaction solution was diluted with saline, and an appropriate dilution of the sample was incubated at 37 °C for 24 h on a Luria–Bertani agar plate. The number of viable cells was then determined by the plate count method.

3. Results and discussion

3.1 Characterization of the prepared photocatalysts

The XRD patterns of the Ag–AgBr/TiO_2 composites (Fig. 1) show the presence of both AgBr and TiO_2 in the systems. Besides the diffraction peaks characteristic of anatase, the peaks at *ca.* 26.7°, 31.0°, 44.4°, 55.0°, 64.5° and 73.4° indexed to AgBr (JCPDS no. 6-438) can be also observed in Ag–AgBr/TiO_2. The XRD pattern of S–Ag–AgBr/TiO_2 is similar to that of Ag–AgBr/TiO_2 but with stronger and sharper diffraction peaks of anatase. It indicates that the solvothermal treatment with elevated temperature and pressure could induce the higher crystallinity and larger crystallite size of anatase in the S–Ag–AgBr/TiO_2. The pure TiO_2 and Ag/TiO_2 were predominantly of anatase phase, and a mixture of anatase, rutile and AgBr was formed in Ag–AgBr/P25. On the other hand, for the samples containing Ag–AgBr, the diffraction peaks at about 44.4° and 64.5° can be assigned to both Ag^0 species and AgBr, while the characteristic peak of Ag^0 species at 38.1° was not found, possibly due to its low content, ultrafine particle size and high dispersion.[11] It is therefore difficult to draw any conclusions regarding the existence of metallic Ag from the XRD measurement only.

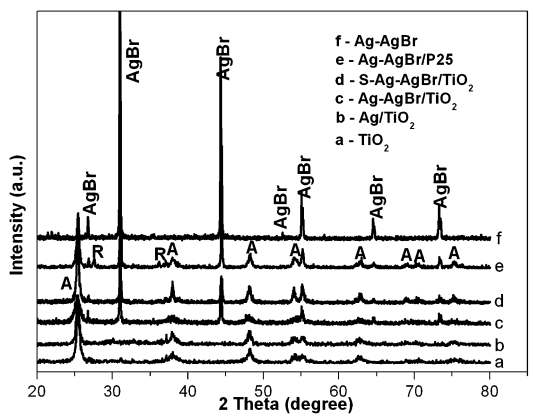

Fig. 1 XRD patterns of the as-prepared photocatalysts, where "A" and "R" represent anatase and rutile respectively.

The synthesized Ag–AgBr/TiO_2 composites were further analyzed by XPS to investigate the elemental composition and chemical states of elements on the surface, as shown in Fig. 2. Besides the C signal, peaks of Ti, O, Ag and Br can be observed in the corresponding samples. Furthermore, peaks of Ag and Br for Ag–AgBr/TiO_2 exhibit higher intensities than S–Ag–AgBr/TiO_2, which reflects higher contents of Ag and Br in the Ag–AgBr/TiO_2 as compared to S–Ag–AgBr/TiO_2. As seen from the high-resolution Ag 3d XPS spectra, Ag/TiO_2 exhibited doublet peaks located *ca.* 374.1 and 368.1 eV corresponding to Ag $3d_{3/2}$ and Ag $3d_{5/2}$ respectively, suggesting that metallic Ag was deposited on the TiO_2 surface.[11,23] For the samples Ag–AgBr/TiO_2 and S–Ag–AgBr/TiO_2, the weak peaks indicative of metallic Ag can be also found. Another pair of peaks appears at around 373.0 and 367.1 eV, which are attributed to Ag^+ of AgBr.[13,23] This result indicates the coexistence of metallic Ag and AgBr in the composites, and Ag species was mainly present as Ag^+. On the contrary, Ag species on the surface of Ag–AgBr were predominantly metallic Ag. XPS spectra of Br 3d for the corresponding samples show one wide peak at *ca.* 68.2 eV, which could be assigned to Br^- in AgBr.[13] The Ti 2p core level for Ag/TiO_2 is slightly shifted towards lower binding energies as compared to TiO_2, while there was no difference between Ag/TiO_2, Ag–AgBr/TiO_2 and S–Ag–AgBr/TiO_2. Hence, the change of Ti state in the TiO_2 might be attributed to the loaded metallic Ag rather AgBr. It implies that TiO_2 might make direct contact with Ag nanoparticles which could be mainly present on the AgBr surface.

The FESEM image of Ag–AgBr/TiO_2 (Fig. 3A) shows that a small fraction of sphere-like particles (appear as bright spots) with diameter of 150–450 nm are homogenously dispersed in the matrix of particles with diameters in the range of 300–450 nm. Similarly, it can be found that the tiny particles (appear as bright spots) are uniformly distributed in the S–Ag–AgBr/TiO_2 but with smaller size (<200 nm) as compared to that in the Ag–AgBr/TiO_2. According to the results of XRD and XPS, the metallic Ag, AgBr and TiO_2 coexist in the Ag–AgBr/TiO_2 composites. EDX spectra of Ag–AgBr/TiO_2 and S–Ag–AgBr/TiO_2 (Fig. 3C and D)

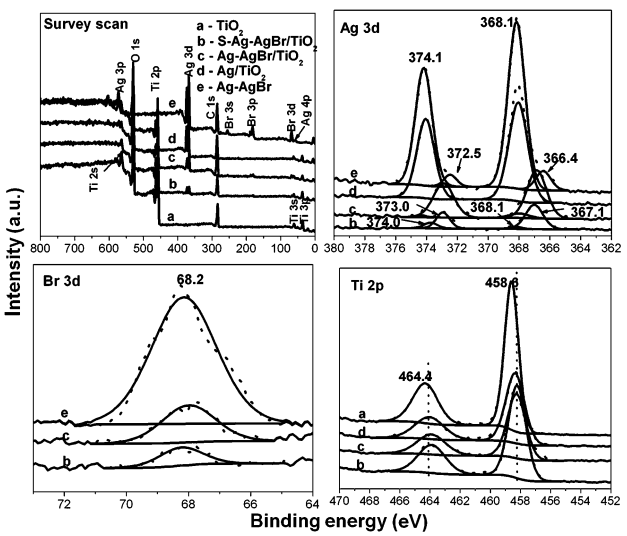

Fig. 2 Survey scan XPS spectra and high-resolution XPS spectra of Ag 3d, Br 3d and Ti 2p regions for the derived photocatalysts.

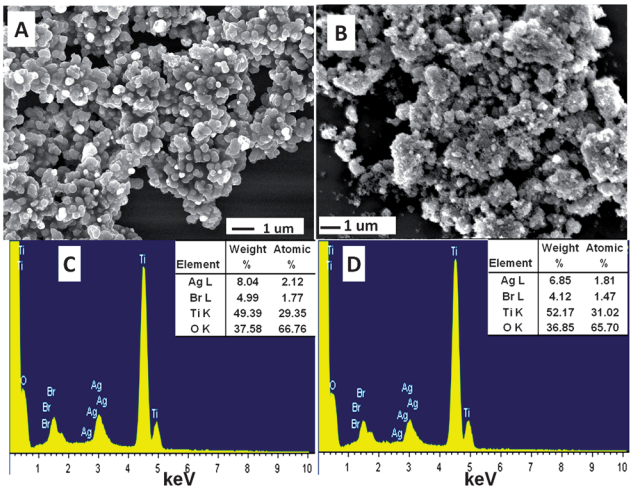

Fig. 3 FESEM images of Ag–AgBr/TiO_2 (A) and S–Ag–AgBr/TiO_2 (B); EDX spectra of Ag–AgBr/TiO_2 (C) and S–Ag–AgBr/TiO_2 (D) and the inset shows the corresponding elemental composition.

clearly reveal the presence of Ag, Br, Ti, and O elements in the composites. The atomic ratio of Ag/Br/Ti/O is 1.00 : 0.83 : 13.84 : 31.53 and 1.00 : 0.81 : 16.59 : 36.3 for Ag–AgBr/TiO_2 and S–Ag–AgBr/TiO_2 respectively. This result also suggests the coexistence of the three components in the Ag–AgBr/TiO_2 composites. Additionally, it indicates that the surface of TiO_2 particles is not completely covered by Ag and AgBr species. Interestingly, Ag/Ti of the Ag–AgBr/TiO_2 obtained by sol–gel method is slightly larger than that of S–Ag–AgBr/TiO_2, which is consistent with that shown in XPS analysis as mentioned above. This result indicates that a relatively lower content of Ag–AgBr is incorporated into TiO_2 particles *via* the solvothermal treatment, possibly owing to the enhanced nucleation and crystallization of anatase TiO_2 from the colloidal $Ti(OH)_4$ under such solvothermal conditions.

TEM images of Ag–AgBr/TiO_2 and S–Ag–AgBr/TiO_2 (Fig. 4A and C) demonstrate the distribution of two kinds of grains in the composites. EDX spectra of Ag–AgBr/TiO_2 for the designated spots (Fig. S1†) reveal that the black spots represent Ag–AgBr, and the dark spots could be assigned to TiO_2. The diameters of Ag–AgBr particles and TiO_2 aggregated particles in the Ag–AgBr/TiO_2 are in the range of 150–350 and 300–500 nm respectively, which are similar to that observed from FESEM image. For the S–Ag–AgBr/TiO_2, EDX spectra and HRTEM images for the designated spots (Fig. S2†) indicate that Ag–AgBr and TiO_2 were present in the composite, and the small particles (as black spots) with mean size of *ca.* 10 nm could be mainly assigned to metallic Ag species, which could originate from AgBr decomposition under the high energy electron beam.[13] Hence, it is difficult to determine the size distribution of individual Ag nanoparticles and AgBr by TEM. These results also imply that the AgBr component in the Ag–AgBr/TiO_2 might be more stable under electron beam irradiation as compared to that in the S–Ag–AgBr/TiO_2. As shown in the insets of Fig. 4A and C, the TiO_2 spheres in the Ag–AgBr/TiO_2 are assembled by fine primary particles with a mean size of <10 nm, and TiO_2 particles in the S–Ag–AgBr/TiO_2 exhibit irregular shapes with sizes in the range of 20–40 nm, which are in good agreement with the average

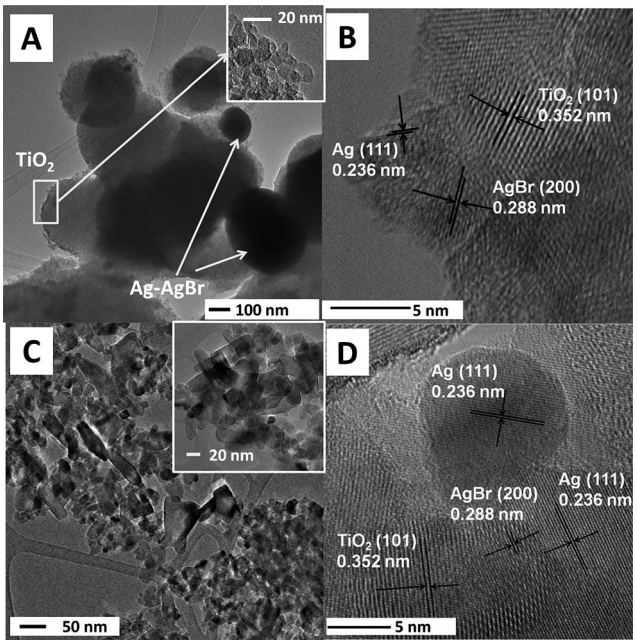

Fig. 4 TEM images of Ag–AgBr/TiO_2 taken at (A) low and (B) high magnifications; TEM images of S–Ag–AgBr/TiO_2 taken at (C) low and (D) high magnifications.

crystallite size of anatase (Table 1, 9.1 and 21.6 nm for Ag–AgBr/TiO_2 and S–Ag–AgBr/TiO_2 respectively) as obtained from XRD measurement. By measuring the lattice fringes as displayed in the HRTEM images of Ag–AgBr/TiO_2 and S–Ag–AgBr/TiO_2 (Fig. 4B and D), the resolved interplanar distances are found to be *ca.* 0.352, 0.288 and 0.236 nm corresponding to the planes of anatase (101) (JCPDS no. 21-1272), AgBr (200) (JCPDS no. 6-438) and Ag (111) (JCPDS no. 65-2871) respectively. It indicates the formation of Ag–AgBr–TiO_2 nanojunctions in the as-synthesized Ag–AgBr/TiO_2 composites.

In addition, as shown in the FESEM image of Ag–AgBr (Fig. S3A†), the Ag–AgBr microspheres are of 2–10 μm, which were much bigger than the Ag–AgBr particles in the Ag–AgBr/TiO_2 composites. It was likely that the surfactant CTAB applied in the synthesis not only supplied the Br^-, but also formed a soft layer surrounding the Ti precursors to control the nucleation sites for AgBr growth.[24] As a result, the Ag–AgBr/TiO_2 composites had the smaller size of AgBr (Ag–AgBr) particles which were evenly distributed in the three-component system.

Based on the above results of XRD, XPS, FESEM and TEM in combination with EDX analyzes for the Ag–AgBr/TiO_2 composites, it can be concluded that the composites were composed of three components (TiO_2, AgBr and metallic Ag), and Ag–AgBr particles were evenly distributed in the matrix of TiO_2 particles. The formation of Ag–AgBr–TiO_2 nanojunctions could be favourable for interfacial charge transfer among the three components, resulting in improved photocatalytic activities of the composites.

UV-vis diffuse reflectance spectra (DRS) of the as-prepared Ag–AgBr/TiO_2 composites and the reference samples such as TiO_2, Ag/TiO_2, Ag–AgBr/P25 and Ag–AgBr are compared in Fig. 5. The prepared TiO_2 exhibited slightly enhanced absorption of visible light (>400 nm) as compared to P25. It has been

Table 1 Crystallite sizes, BET surface areas of photocatalysts and their TOC removal efficiencies of IBP, Ag^+ released after 6 h of visible light irradiation

Photocatalyst	Crystallite size[a] (nm)		S_{BET}[b] ($m^2\ g^{-1}$)	TOC removal at 6 h (%)	Ag^+ in IBP solutions at 6 h ($\mu g\ L^{-1}$) (%)[c]
	Anatase	AgBr			
Ag–AgBr/TiO_2	9.1	38.6	32.4	81	<10 (~0.01%)
S–Ag–AgBr/TiO_2	21.6	37.6	39.9	79	<10 (~0.01%)
Ag–AgBr/P25	23.8	38.7	23.1	43	<10 (~0.01%)
Ag–AgBr	—	42.5	<D.L.[d]	36	<10 (~0.01%)
Ag/TiO_2	18.2	—	38.7	23	4392 (9.30%)
TiO_2	14.5	—	117.1	26	—

[a] Derived from XRD patterns. [b] BET surface area. [c] Weight percentage of soluble Ag^+ relative to total Ag in the photocatalysts (which were determined by EDX analysis). [d] Detection limit.

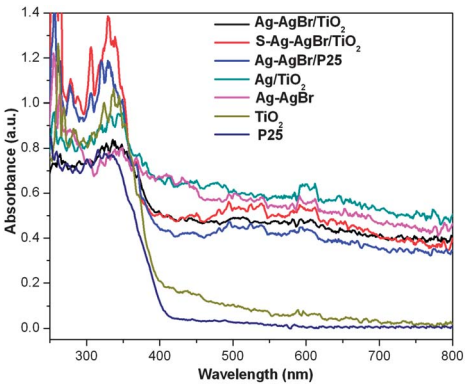

Fig. 5 UV-vis diffuse reflectance spectra of the synthesized photocatalysts and P25.

reported that the calcination process might induce a number of oxygen vacancies on the surface of TiO_2,[25] which could be responsible for its ability to absorb visible-light. For Ag/TiO_2, absorption toward visible light is remarkably enhanced in comparison with TiO_2, but there is almost no shift of absorption edge. This could be due to the SPR of Ag nanoparticles,[26] since metallic Ag was present on the surface of Ag/TiO_2 as proved by XPS analysis. Ag–AgBr exhibited strong absorption in the visible light region, resulting from the SPR of Ag nanoparticles and the visible-light absorption of AgBr which has an indirect band gap of 2.6 eV. Therefore, the incorporation of Ag–AgBr in the Ag–AgBr/TiO_2 composites resulted in the noticeable red shift of absorption edge as well as the enhancement of absorption ability of visible light.

Fig. 6 shows the PL spectra of the as-synthesized TiO_2-based photocatalysts. It can be found that the PL intensity of pure TiO_2 significantly decreases with the introduction of Ag or Ag–AgBr. Moreover, Ag–AgBr/TiO_2 exhibits lower PL intensity than that of Ag/TiO_2. It has been accepted that the Schottky barrier formed at the Ag–TiO_2 interface could act as an efficient electron trap suppressing the electron–hole recombination for Ag/TiO_2.[27] Furthermore, the vectorial electron transfer could occur in the TiO_2–Ag–AgBr nanojunction system, which could greatly enhance the interfacial charge transfer and facilitate the separation of charge carriers. As a result, the Ag–AgBr/TiO_2 three-component system exhibited a decreased electron–hole recombination rate as compared to single-component (TiO_2) and two-component (Ag–TiO_2) systems. There could be several factors influencing the recombination of photoinduced charge carriers in the Ag–AgBr/TiO_2 three-component system, such as content of Ag–AgBr, homogeneity of the Ag–AgBr dispersion and nanostructure of the composites. PL intensities of the Ag–AgBr/TiO_2 and S–Ag–AgBr/TiO_2 are lower than that of conventional Ag–AgBr/P25, which could be attributed to the even distribution of Ag–AgBr particles in the matrix of TiO_2 particles and formation of TiO_2–Ag–AgBr nanojunctions for the synthesized Ag–AgBr/TiO_2 composites. On the other hand, in comparison with the solvothermally synthesized S–Ag–AgBr/TiO_2, the higher content of Ag–AgBr incorporated into the Ag–AgBr/TiO_2 could result in the more efficient transfer of charge carriers. This could be the reason for the lower PL intensity of the Ag–AgBr/TiO_2 than that of S–Ag–AgBr/TiO_2.

3.2 Photocatalytic degradation of IBP, aromaticity of byproducts and toxicity during IBP degradation

Photocatalytic degradation (PCD) of IBP over the as-prepared photocatalysts under white LED irradiation is shown in Fig. 7. Photolysis of IBP throughout 2 h of irradiation was negligible. P25 was almost inactive for degradation of IBP under white LED irradiation. Generally the three-component composites (Ag–AgBr/TiO_2, S–Ag–AgBr/TiO_2 and Ag–AgBr/P25) exhibited enhanced photocatalytic performance towards IBP degradation as compared to the single and two-component systems. Moreover, both Ag–AgBr/TiO_2 and S–Ag–AgBr/TiO_2 showed much higher PCD efficiencies than Ag–AgBr/P25. Among the as-prepared photocatalysts, the highest IBP removal rate was

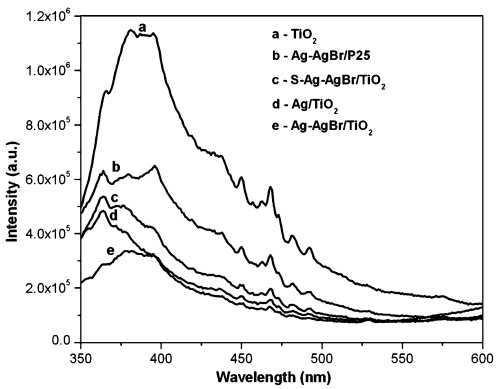

Fig. 6 PL spectra of the derived photocatalysts.

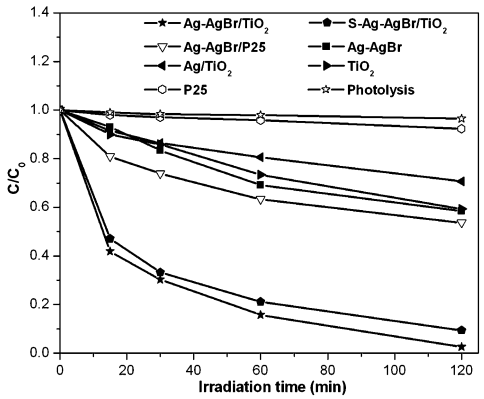

Fig. 7 Photocatalytic activities of the synthesized photocatalysts for IBP degradation under white LED irradiation.

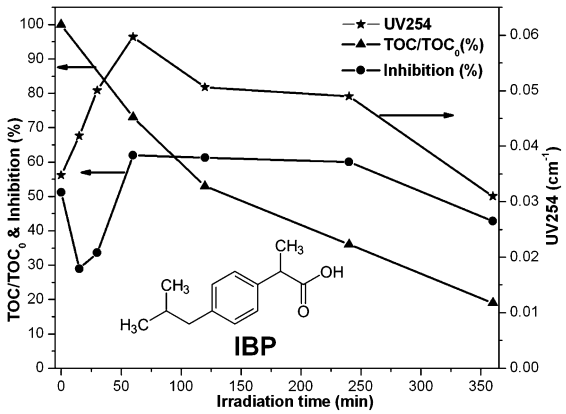

Fig. 8 Evolution of TOC, UV_{254} and toxicity of IBP solutions during the process of IBP degradation under white LED irradiation.

observed in the Ag–AgBr/TiO_2, whereby 98% of IBP was decomposed after 2 h of white LED irradiation. Since the S_{BET} of Ag–AgBr/TiO_2 composites and Ag/TiO_2 are quite close and much smaller than that of TiO_2 (Table 1), the outstanding visible-light photocatalytic activity of Ag–AgBr/TiO_2 could be mainly attributed to the following factors. Firstly, both Ag and AgBr can be excited under white LED irradiation, leading to the enhanced utilization of visible light. Secondly, the three-component systems especially those with well-dispersed nano-junctions between Ag–AgBr and TiO_2 could be more efficient for charge transfer and separation of photoexcited electron–hole pairs. However, for the Ag/TiO_2, although it had better abilities for visible light absorption (Fig. 5) and separation of charge carriers (Fig. 6) as compared to S–Ag–AgBr/TiO_2 and Ag–AgBr/P25, it exhibited much lower visible-light photocatalytic activities for IBP removal. This could be due to its poor photostability during the visible-light photocatalytic process, owing to the release of oxidized Ag^+ ions in water (discussed later). Therefore, the high stability of the Ag–AgBr/TiO_2 due to the Ag–AgBr/TiO_2 nanojunction structure could also be crucial for achieving a high PCD efficiency. In addition, the visible-light photocatalytic activity of Ag–AgBr was lower than that of Ag–AgBr/TiO_2. These results reveal that each component in the Ag–AgBr/TiO_2 composites could play an important role in its visible-light photocatalytic activity.

As presented in Fig. 8, the TOC of IBP solution continued to decrease with increasing irradiation time. The TOC removal rate was far lower than that of IBP degradation, which could be attributed to generation of more persistent intermediates. However TOC might be completely decomposed with further irradiation. The formation of intermediates can be confirmed from the time-dependent HPLC profiles of IBP during the course of the photocatalytic process (Fig. S4†). A similar phenomenon can be found in the UV-vis absorption spectra of IBP during the IBP mineralization (Fig. S4†).

Since UV absorbance at 254 nm (UV_{254}) is closely related to the concentration of organic molecules with aromatic grouping or extended conjugation, it has been used as an indicator of aromaticity of organic substance.[28] The time-course of UV_{254} during IBP degradation is illustrated in Fig. 8. UV_{254} of IBP solution was elevated during the initial 60 min and reached a peak value, thereafter deceased to a lower level at 360 min than the initial value. The result indicates that PCD of the aliphatic moieties of the IBP occurred prior to the aromatic ring-cleavage reaction. A small amount of formic acid was indeed detected in the IBP solution after 360 min of irradiation with white LED.

In view of the generation of intermediates during the course of IBP mineralization which might be more toxic than the parent IBP, it is significant to evaluate the evolution of solution toxicity upon IBP degradation. The inhibition of the bioluminescence of *V. fischeri* indicates sample's toxicity level. Fig. 8 shows that toxicity slightly decreased at the beginning of photocatalytic reaction because of IBP removal, then increased until a maximum value at 60 min due to formation of hydroxylated metabolites of IBP,[19,29] and subsequently decreased with the extended irradiation time. The toxicity became lower than that of the initial IBP solution after 360 min of white LED irradiation.

3.3 Antibacterial activities of Ag–AgBr/TiO_2 composites

As shown in Fig. 9, pure TiO_2 and conventional Ag–AgBr/P25 in the dark exhibited very weak antibacterial effects on *E. coli*. The Ag–AgBr/semiconductor (such as WO_3,[13] Bi_2WO_6,[30] *etc.*) photocatalysts as reported in literature were also not toxic to *E. coli* in the dark. However, 77% and 56% of the bacterial cells were

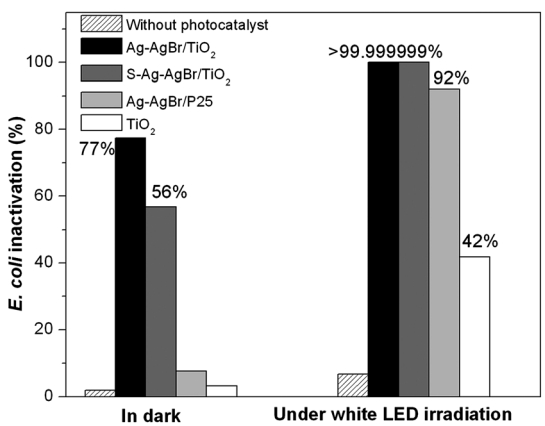

Fig. 9 Antibacterial activities of the prepared photocatalysts (0.05 g L^{-1}) against *E. coli* in the dark and under white LED irradiation within 1 h.

inactivated by the synthesized Ag–AgBr/TiO_2 and S–Ag–AgBr/TiO_2 composites in the dark within 60 min. Silver has been widely used as an antibacterial agent. It has been reported that both ionic and metallic silver exhibit antibacterial activities.[31] The release of Ag^+ from the Ag–AgBr/TiO_2 composites in the dark was monitored using inductively coupled plasma optical emission spectroscopy (ICP-OES, Perkin Elmer Optima 2000DV). It is found that the concentrations of dissolved Ag^+ from the composites were extremely low. Therefore, it suggests that the antibacterial activities of the Ag–AgBr/TiO_2 composites in the dark could be mainly attributed to the evenly dispersed metallic Ag nanoparticles in the systems. It is reasonable that the Ag–AgBr/TiO_2 with a higher content of metallic Ag exhibited slightly stronger antibacterial activity in the dark than that of S–Ag–AgBr/TiO_2. As a result of various reactive oxygen species ($O_2^{\cdot-}$, $^{\cdot}OH$, H_2O_2, *etc.*) generated on the visible-light-irradiated photocatalysts, *E. coli* inactivation over these photocatalysts was generally enhanced under white LED irradiation. Similarly to the results of IBP degradation, the Ag–AgBr/TiO_2 composites showed much higher efficiency of *E. coli* inactivation than the pure TiO_2 and conventional Ag–AgBr/P25, whereby complete *E. coli* inactivation of >6 log was achieved after 60 min of irradiation. Furthermore, an increase of Ag–AgBr/TiO_2 dosage (in the range of 0.025–0.25 g L^{-1}) resulted in the increased antibacterial activities in the dark and under white LED irradiation (Fig. 10). As a result, in comparison with TiO_2 and conventional Ag–AgBr/P25 photocatalysts, the Ag–AgBr/TiO_2 could be a more promising antibacterial agent which can be used in both dark and visible light conditions.

3.4 Stability and reusability of the as-prepared photocatalysts

The photochemical stability of the as-prepared photocatalysts was evaluated by monitoring the dissolved Ag^+ during IBP degradation under white LED irradiation. The IBP solutions were analyzed for dissolved Ag^+ throughout the photocatalytic process using ICP-OES. As shown in Table 1, the Ag^+ ions released from the three-component composites and Ag–AgBr are negligible. However, when Ag/TiO_2 was used, 9.30 wt% of total Ag was released after 6 h of white LED irradiation, indicating that the oxidation of Ag nanoparticles occurred due to the plasmon-induced charge separation. The stability of these photocatalysts could be strongly associated with the charge transfer mechanism in the composites. In addition, the XRD patterns (Fig. S5†) and Ag 3d, Br 3d and Ti 2p XPS spectra (Fig. S6†) of the Ag–AgBr/TiO_2 composites after photocatalytic reactions are almost identical to those of fresh samples, which prove that the crystal structure and surface chemical composition of the Ag–AgBr/TiO_2 composites did not change throughout the photocatalytic process. The Ag–AgBr/TiO_2 was further evaluated for its durability for IBP degradation. This photocatalyst was reused after simple filtration and washing with DI water. Fig. 11 shows that the Ag–AgBr/TiO_2 composite still exhibited high visible-light photocatalytic performance for IBP removal even after the fifth consecutive run. Based upon the above results, it is concluded that the Ag–AgBr/TiO_2 composites were quite stable under the experimental conditions.

3.5 Proposed mechanisms for high stability and visible-light photocatalytic activity

3.5.1 Action spectrum of the Ag–AgBr/TiO_2. Ag nanoparticles exhibit SPR in the visible and near-infrared regions,[8] and AgBr can be excited by light with wavelengths less than *ca.* 477 nm.[11] Hence, both SPR of Ag nanoparticles and excitation of AgBr could occur in the Ag–AgBr/TiO_2 system under visible light (λ > 400 nm) irradiation. To gain further insight into the roles of Ag nanoparticles and AgBr in the visible-light photocatalytic activity of the Ag–AgBr/TiO_2 composite, PCD of IBP by the photocatalyst under irradiation with different LED (quasi-monochromatic) lights was carried out in this study. To our best knowledge, the action spectrum of Ag–AgX based photocatalysts investigated using various monochromatic lights has not been reported. As shown in Fig. 12, 98%, 97%, 80% and 62% of IBP were degraded by the Ag–AgBr/TiO_2 within 2 h under irradiation with white, blue, green and yellow LEDs respectively, with concomitant TOC removal of 81%, 80%, 60% and 45% after 6 h irradiation. The irradiation with white and blue LED resulted in higher IBP removal efficiencies than those of green and yellow LEDs. This is possibly because both Ag nanoparticles and AgBr were photoactive under white (which emits blue light and broadband light of around 500–600 nm) and

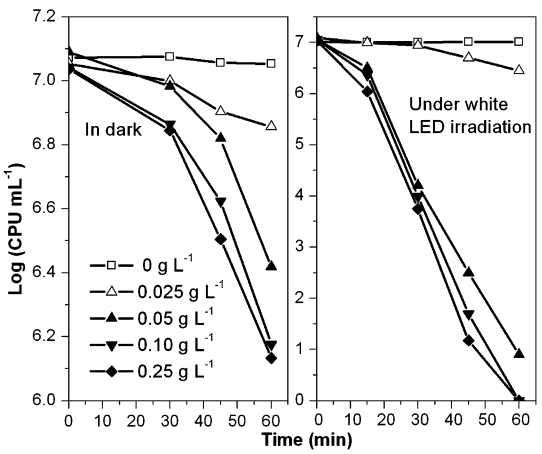

Fig. 10 Effect of Ag–AgBr/TiO_2 dosage on the *E. coli* inactivation in the dark and under white LED irradiation.

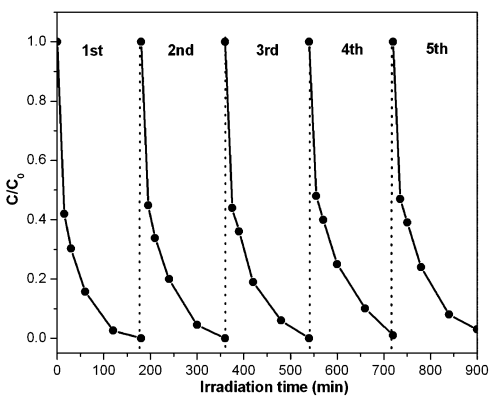

Fig. 11 Cycling runs in the photocatalytic degradation of IBP using Ag–AgBr/TiO_2 under white LED irradiation.

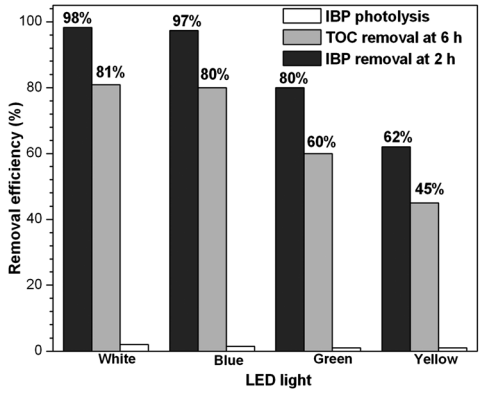

Fig. 12 IBP and TOC removal efficiencies under different colors of LED irradiation.

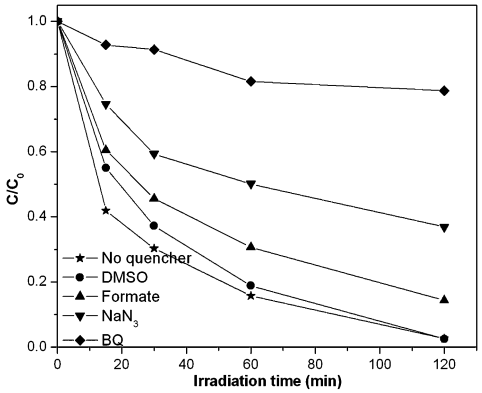

Fig. 13 Photocatalytic degradation of IBP by Ag–AgBr/TiO_2 without and with the presence of various scavengers.

blue LED ($\lambda = 465$ nm) irradiation, while Ag nanoparticles were the only photoactive species under green ($\lambda = 523$ nm) and yellow ($\lambda = 589$ nm) LED irradiation. The Ag–AgBr/TiO_2 still achieved relatively high IBP removal efficiency even under yellow LED irradiation. This result proves that besides AgBr, SPR of Ag nanoparticles could also contribute to the visible-light photocatalytic activity of the synthesized Ag–AgBr/TiO_2.

3.5.2 Roles of oxidative species in IBP degradation upon the Ag–AgBr/TiO_2. The generation and roles of reactive oxidative species, such as h^+, $^{\cdot}OH$, $O_2^{\cdot-}$ and $^1O_2$, in the PCD of IBP were investigated indirectly with the use of appropriate quenchers of these species. Formate has been found to be an effective hole scavenger for TiO_2-based photocatalysts.[32] It is also capable of scavenging the photoproduced holes in AgBr crystals to form $CO_2^{\cdot-}$, since the redox potential of valence band hole of AgBr (+1.6 V *vs.* normal hydrogen electrode (NHE)) is more positive than that of E^0 ($CO_2^{\cdot-}/HCO_2^-$) (1.07 V).[33] In addition, dimethyl sulfoxide (DMSO), benzoquinone (BQ) and NaN_3 were used as quenchers of $^{\cdot}OH$, $O_2^{\cdot-}$ and $^1O_2$ respectively. The efficiencies of IBP degradation without any quenchers and with the presence of 0.1 mM of DMSO, formate, NaN_3 and BQ under identical conditions are compared in Fig. 13. Addition of DMSO caused a slight reduction in IBP removal efficiency, whereas IBP degradation was remarkably depressed with the presence of formate, NaN_3 and BQ. The inhibition of IBP degradation was the most pronounced with the addition of BQ. According to the above observations, it can be deduced that h^+, $^{\cdot}OH$, $O_2^{\cdot-}$ and $^1O_2$ were involved in PCD of IBP over the Ag–AgBr/TiO_2 composite, and $O_2^{\cdot-}$ was the predominant reactive species.

3.5.3 Proposed mechanisms. The possible mechanisms for the high stability and visible-light photocatalytic activity of the Ag–AgBr/TiO_2 are proposed (Fig. 14). Accordingly, the relevant reactions occurring at the composite surface involved in the IBP degradation process under visible-light LED irradiation are listed in Table 2. Considering that the visible-light response of TiO_2 was far weaker than the other two components, to simplify the mechanism, the formation of oxygen vacancies on the TiO_2 surface was not reflected in the schematic diagram.

Under white LED irradiation, both Ag nanoparticles and AgBr were the photoactive species (Fig. 14A). Because of the dipolar character of the SPR of Ag nanoparticles, the photo-induced plasmons on the surface of Ag nanoparticles could decay into charge carriers, *i.e.*, electrons and holes.[34] The mechanism of charge transfer in the plasmonic photocatalysts Ag–TiO_2 or Ag–AgBr is different from the traditional metal–semiconductor Schottky barrier that hinders the migration of electrons from metal to semiconductor.[35] It has been proven that the energetic electrons from the plasmon-excited Ag nanoparticles can inject into the conduction band (CB) of TiO_2 and AgBr or tunnel through the Schottky barriers at the interface of Ag–TiO_2 and Ag–AgBr.[14,36] For the synthesized Ag–AgBr/TiO_2 composite, the plasmon-induced electrons on Ag nanoparticles might flow to the CB of TiO_2 rather than AgBr, owing to the less negative CB edge of TiO_2 (−0.10 V *vs.* NHE) as compared to that of AgBr (−1.04 V *vs.* NHE). Meanwhile, the plasmon-induced holes would migrate away from the Ag and be trapped within the surface of

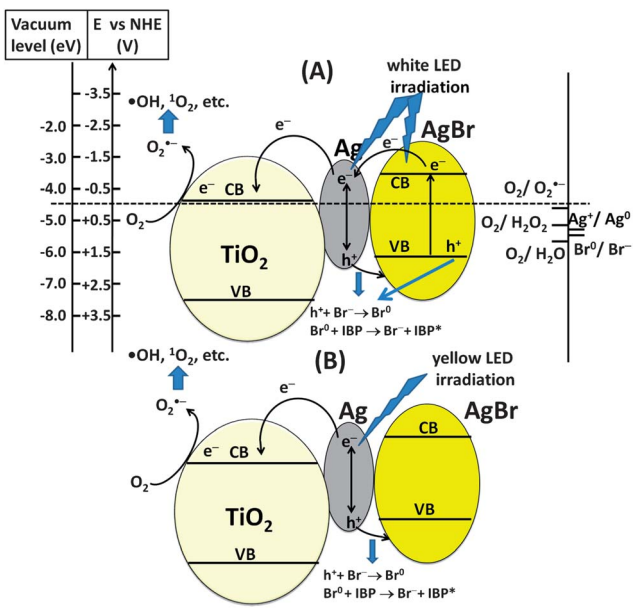

Fig. 14 Proposed photocatalytic mechanisms over the Ag–AgBr/TiO_2 under visible-light LED irradiation. The standard potentials of several redox couples associated with the photocatalytic reactions are shown on the right scale.

Table 2 Relevant reactions occurring at the surface of Ag–AgBr/TiO_2 composite involved in the IBP degradation process, under visible-light LED irradiation

Reactions	No.
$AgBr + h\nu \rightarrow AgBr(e^- + h^+)$	(1)
$Ag + h\nu \rightarrow Ag^*$	(2)
$Ag^* + TiO_2 \rightarrow TiO_2(e^-) + Ag^{+\cdot}$	(3)
$AgBr(e^- + h^+) + TiO_2 \rightarrow AgBr(h^+) + TiO_2(e^-)$	(4)[a]
$TiO_2(e^-) + O_2 \rightarrow O_2^{\cdot -} + TiO_2$	(5)
$O_2^{\cdot -} + H^+ \rightarrow HO_2^{\cdot}$	(6)
$HO_2^{\cdot} + TiO_2(e^-) + H^+ \rightarrow H_2O_2 + TiO_2$	(7)
$H_2O_2 + TiO_2(e^-) \rightarrow {}^{\cdot}OH + OH^- + TiO_2$	(8)
$O_2^{\cdot -} + {}^{\cdot}OH \rightarrow {}^1O_2 + OH^-$	(9)
$Ag^+/AgBr(h^+) + Br^- \rightarrow Ag/AgBr + Br^0$	(10)
$Br^0 + IBP \rightarrow IBP^* + Br^-$	(11)
$O_2^{\cdot -}$, $^1O_2$, $AgBr(h^+)$, ${}^{\cdot}OH + IBP \rightarrow$ mineralization products	(12)

[a] Ag nanoparticles acted as electron-transfer media.

AgBr particles,[11,18] leading to the efficient charge separation in the Ag nanoparticles. Besides, the electrons from the photoexcited AgBr could be injected into the Ag and could immediately transfer to the CB of TiO_2. The electron migration away from AgBr could significantly inhibit the reaction where Ag^+ of AgBr might capture conduction-band electrons, which could cause the decomposition of AgBr into Ag^0. The electrons in the CB of TiO_2 from photoexcited AgBr and plasmon-excited Ag nanoparticles can be subsequently trapped by the absorbed O_2 to form $O_2^{\cdot -}$ (eqn (5)) and other oxidative species such as ${}^{\cdot}OH$ and $^1O_2$ (eqn (6)–(9)). The reactive species including $O_2^{\cdot -}$, ${}^{\cdot}OH$ and $^1O_2$ were then utilized for IBP degradation. On the other hand, the photoproduced holes on AgBr could oxidize IBP directly. Additionally, the transferred holes from Ag nanoparticles and photoproduced holes on AgBr would interact with Br^- in AgBr to form Br^0, and Br^0 is able to oxidize IBP while being reduced to Br^- again.[18] Therefore, in this Ag–AgBr/TiO_2 composite, plasmon-excited Ag nanoparticles served as electron-transfer media, while TiO_2 also participated in the charge transfer besides serving as support for Ag–AgBr. The vectorial electron transfer of AgBr → Ag → TiO_2 occurring in the Ag–AgBr/TiO_2 composite could greatly enhance the interfacial charge transfer, meanwhile ensure the high stability of the composite.

Under yellow LED irradiation, Ag nanoparticles were the only photoactive species responsible for the visible-light photocatalytic performance of the composite. The behaviour of the SPR-induced charge transfer could be similar to that under white LED irradiation (Fig. 14B).

4. Conclusions

The highly visible-light photoactive Ag–AgBr/TiO_2 composites were fabricated *via* a one-pot synthesis. The Ag–AgBr particles with high uniformity were evenly distributed in the matrix of TiO_2 particles, leading to the formation of nanojunction between Ag–AgBr and TiO_2. Owing to coexistence of two visible-light active components (Ag nanoparticles and AgBr) and the effective separation and transportation of charge carriers in the Ag–AgBr/TiO_2 composite, the three-component system exhibited enhanced visible-light photocatalytic activities for IBP degradation as compared to the single-component and two-component systems, as well as the conventional Ag–AgBr/P25 composite. Meanwhile the Ag–AgBr/TiO_2 was highly efficient for *E. coli* inactivation under white LED irradiation. More specially, different from the Ag–AgBr/semiconductor photocatalysts that have been reported in literature, the heterostructured Ag–AgBr/TiO_2 exhibited novel antibacterial activities against *E. coli* in the dark. This study signifies that the highly efficient and stable Ag–AgBr/TiO_2 composite could be a promising photocatalyst and antibacterial agent that can be used for the destruction of organic contaminants and bacteria under indoor and sunlight irradiation.

Acknowledgements

The National Research Foundation (NRF) and Nanyang Technological University of Singapore are hereby acknowledged for their financial support. The authors would like to thank Ms Liew Ming Yian for her technical assistance in PL measurement.

References

1 X. Chen and S. S. Mao, *Chem. Rev.*, 2007, **107**, 2891–2959.
2 G. Liu, L. Wang, H. G. Yang, H. M. Cheng and G. Q. Lu, *J. Mater. Chem.*, 2010, **20**, 831–843.
3 B. Ohtani, *Recent Pat. Eng.*, 2010, **4**, 149–154.
4 P. Wang, B. Huang, X. Qin, X. Zhang, Y. Dai, J. Wei and M. H. Whangbo, *Angew. Chem., Int. Ed.*, 2008, **47**, 7931–7933.
5 K. Awazu, M. Fujimaki, C. Rockstuhl, J. Tominaga, H. Murakami, Y. Ohki, N. Yoshida and T. Watanabe, *J. Am. Chem. Soc.*, 2008, **130**, 1676–1680.
6 J. F. Guo, B. W. Ma, A. Y. Yin, K. N. Fan and W. L. Dai, *Appl. Catal., B*, 2011, **101**, 580–586.
7 D. Chen, S. H. Yoo, Q. Huang, G. Ali and S. O. Cho, *Chem.–Eur. J.*, 2012, **18**, 5192–5200.
8 M. Rycenga, C. M. Cobley, J. Zeng, W. Li, C. H. Moran, Q. Zhang, D. Qin and Y. Xia, *Chem. Rev.*, 2011, **111**, 3669–3712.
9 J. N. Anker, W. P. Hall, O. Lyandres, N. C. Shah, J. Zhao and R. P. Van Duyne, *Nat. Mater.*, 2008, **7**, 442–453.
10 L. Kuai, B. Y. Geng, X. T. Chen, Y. Y. Zhao and Y. C. Luo, *Langmuir*, 2010, **26**, 18723–18727.
11 Y. Hou, X. Y. Li, Q. D. Zhao, X. Quan and G. H. Chen, *J. Mater. Chem.*, 2011, **21**, 18067–18076.
12 L. Zhang, K. H. Wong, Z. Chen, J. C. Yu, J. Zhao, C. Hu, C. Y. Chan and P. K. Wong, *Appl. Catal., A*, 2009, **363**, 221–229.
13 P. Wang, B. Huang, X. Qin, X. Zhang, Y. Dai and M. H. Whangbo, *Inorg. Chem.*, 2009, **48**, 10697–10702.
14 C. Hu, T. Peng, X. Hu, Y. Nie, X. Zhou, J. Qu and H. He, *J. Am. Chem. Soc.*, 2010, **132**, 857–862.
15 H. Tada, T. Mitsui, T. Kiyonaga, T. Akita and K. Tanaka, *Nat. Mater.*, 2006, **5**, 782–786.
16 C. Hu, Y. Q. Lan, J. H. Qu, X. X. Hu and A. M. Wang, *J. Phys. Chem. B*, 2006, **110**, 4066–4072.
17 G. Tian, Y. Chen, H. L. Bao, X. Meng, K. Pan, W. Zhou, C. Tian, J. Q. Wang and H. Fu, *J. Mater. Chem.*, 2012, **22**, 2081–2088.
18 J. Yu, G. Dai and B. Huang, *J. Phys. Chem. C*, 2009, **113**, 16394–16401.
19 F. Méndez-Arriaga, S. Esplugas and J. Giménez, *Water Res.*, 2008, **42**, 585–594.
20 A. Achilleos, E. Hapeshi, N. P. Xekoukoulotakis, D. Mantzavinos and D. Fatta-Kassinos, *Sep. Sci. Technol.*, 2010, **45**, 1564–1570.
21 X. P. Wang and T. T. Lim, *Appl. Catal., B*, 2010, **100**, 355–364.
22 X. P. Wang and T. T. Lim, *Appl. Catal., A*, 2011, **399**, 233–241.
23 Y. Li, H. Zhang, Z. Guo, J. Han, X. Zhao, Q. Zhao and S. J. Kim, *Langmuir*, 2008, **24**, 8351–8357.
24 X. Lu, H. Mao and W. Zhang, *Nanotechnology*, 2007, **18**, 1–5.
25 J. Shi, J. Chen, Z. Feng, T. Chen, Y. Lian, X. Wang and C. Li, *J. Phys. Chem. C*, 2007, **111**, 693–699.
26 H. Zhang, X. Fan, X. Quan, S. Chen and H. Yu, *Environ. Sci. Technol.*, 2011, **45**, 5731–5736.
27 A. L. Linsebigler, G. Lu and J. T. Yates Jr, *Chem. Rev.*, 1995, **95**, 735–758.

28 X. Huang, M. Leal and Q. Li, *Water Res.*, 2008, **42**, 1142–1150.
29 F. Méndez-Arriaga, S. Esplugas and J. Giménez, *Water Res.*, 2010, **44**, 589–595.
30 L. S. Zhang, K. H. Wong, H. Y. Yip, C. Hu, J. C. Yu, C. Y. Chan and P. K. Wong, *Environ. Sci. Technol.*, 2010, **44**, 1392–1398.
31 M. Rai, A. Yadav and A. Gade, *Biotechnol. Adv.*, 2009, **27**, 76–83.
32 A. J. Hoffman, E. R. Carraway and M. R. Hoffmann, *Environ. Sci. Technol.*, 1994, **28**, 776–785.
33 J. Belloni, M. Treguer, H. Remita and R. De Keyzer, *Nature*, 1999, **402**, 865–866.
34 M. Moskovits, *Science*, 2011, **332**, 676–677.
35 Y. Tang, Z. Jiang, J. Deng, D. Gong, Y. Lai, H. T. Tay, I. T. K. Joo, T. H. Lau, Z. Dong and Z. Chen, *ACS Appl. Mater. Interfaces*, 2012, **4**, 438–446.
36 Q. Xiang, J. Yu, B. Cheng and H. C. Ong, *Chem.–Asian J.*, 2010, **5**, 1466–1474.

